Inorganic Chemistry

pubs.acs.org/IC Article

Long-Range Ferromagnetic Exchange Interactions Mediated by Mn-Ce^{IV}-Mn Superexchange Involving Empty 4f Orbitals

Sayak Das Gupta, Robert L. Stewart, Dian-Teng Chen, Khalil A. Abboud, Hai-Ping Cheng, Stephen Hill, and George Christou*



Cite This: Inorg. Chem. 2020, 59, 8716-8726



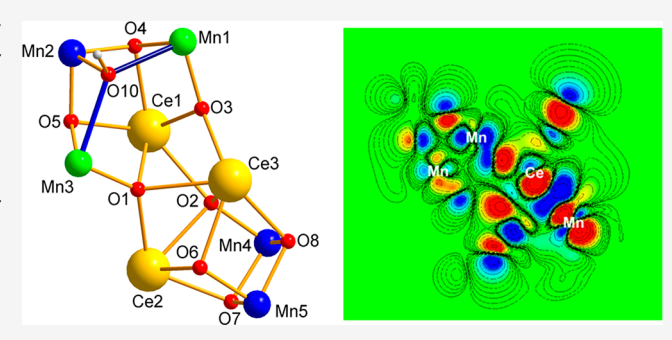
ACCESS

III Metrics & More

Article Recommendations

Supporting Information

ABSTRACT: Reactions involving reductive aggregation of MnO_4^- in methanol in the presence of Ce^{IV} and an excess of carboxylic acid have led to the synthesis of structurally related Ce/Mn clusters, $[Ce_3Mn_5O_8(OMe)(O_2CBu^t)_{13}(MeOH)]$ (1) and $[Ce_2Mn_3O_5(O_2CPh)_9(MeOH)_3]$ (2), containing at least one $\{Mn_2Ce_2O_4\}$ cubane unit. The cores of both clusters contain Mn_x units separated by three (1) or two (2) Ce^{IV} ions. Fits of variable-temperature, solid-state dc and ac magnetic susceptibility data reveal dominant ferromagnetic interactions within 1 and 2, resulting in the maximum $S = {}^{17}/{}_2$ and S = 5 ground state spins, respectively, and thus suggesting significant ferromagnetic (F) interactions between the Mn_x units that are ≥ 6 Å apart and



separated by four intervening bonds through diamagnetic Ce^{IV}. Fits of magnetic susceptibility data also revealed unusual long-range F interactions, and this finding was further supported by high-field EPR measurements and simulations. Density functional theory calculations and a Wannier function analysis confirm long-range interactions and indicate a Mn–Ce–Mn superexchange pathway via Mn-d/Ce-f orbital overlap/hybridization

■ INTRODUCTION

It could not have been predicted when Ce/Mn oxo clusters were first reported in 20031 just how greatly this field would expand in subsequent years and how interesting it would become. Since Ce-O²⁻ chemistry is dominated by the very oxophilic and diamagnetic Ce^{IV} oxidation state, the primary stimulus of the original work was not just molecular magnetism but some other areas as well. In particular, Ce/Mn composite oxides are used in a variety of industrial and catalytic applications such as, for example, environmental abatement of wastewater pollution by catalytic wet oxidation (CWO) of dissolved organic and inorganic pollutants^{2,3} and low temperature oxidation of phenol. 4,5 Once Ce/Mn clusters became available, 1,6 both new single-molecule magnets (SMMs) and catalysts ensued, such as the identification of $[Ce^{IV}Mn^{III}_{8}O_{8}(O_{2}CMe)_{12}(H_{2}O)_{4}]$ with S = 16 as the first Ce/Mn SMM⁶ and the use of [Ce^{IV}Mn^{IV}₆O₉(O₂CMe)₉(NO₃)- $(H_2O)_2$] for catalytic oxidation of benzyl alcohol to benzaldehyde.

Ce/Mn-oxo chemistry has now grown extensively and spans clusters with a large variety of total metal nuclearities and Ce/Mn ratios, from mainly Ce to mainly Mn, and everything in between; some of these also contain one or more Ce^{III} ions. $[Ce_{10}Mn_8O_{18}(O_2C^iPr)_{26}(H_2O)_2]^{11} \text{ and } [Ce_5Mn_{11}O_{13}(OH)_2(O_2CPh)_{24}(NO_3)_2]^{-12} \text{ are the highest nuclearity clusters to date. Several synthetic procedures were$

developed for the reported clusters spanning various Mn and Ce reagents and reaction conditions.

In the present report, we describe application of a new synthetic procedure to Ce/Mn oxo clusters. This is "reductive aggregation," which we originally developed in homometallic Mn chemistry and which involves the methanolysis-driven reduction and concomitant aggregation of MnO₄⁻ ions in MeOH in the presence of excess carboxylic acid. This proved to be a rich source of new Mn_x (x usually is 12 or 16) clusters, the first being $[Mn_{12}O_{12}(OMe)_2(O_2CPh)_{16}(H_2O)_2]^{2-13}$ a distinct structural variant of the prototypical SMM [Mn₁₂O₁₂(O₂CMe)₁₆(H₂O)₄].¹⁴ Reductive aggregation employs a single high oxidation source of Mn, and the MeOH has a multifunctional role as the solvent, the reducing agent, and a source of alkoxide ligands. Depending on the carboxylic acid employed, a number of new structural types of Mn₁₂ and Mn₁₆ clusters were obtained, 15 many of them new SMMs, including an unusual and highly symmetrical "W-shaped" $[Mn_{16}O_{16}(OMe)_6(O_2CPh)_{12}(NO_3)_4(MeOH)_2(H_2O)_4].$

Received: February 1, 2020 Published: June 23, 2020





We thus decided to apply for the first time the reductive aggregation procedure to heterometallic chemistry and chose Ce/Mn chemistry. This has led to the synthesis of Ce₃Mn₅ and Ce₂Mn₃ products, which in addition also exhibit unusual magnetic properties that are a main focus of this report. In particular, they both display unusual ferromagnetic (F) longrange interactions between their two component Mn_x units that are well separated by the diamagnetic Ce^{IV} ions, and we have therefore sought to identify the origin of this interaction. Herein, we report the results of this study, which includes magnetic, spectroscopic, and computational characterization of [Ce₃Mn₅O₈(OMe)(O₂CBu^t)₁₃(MeOH)] (1) and [Ce₂Mn₃O₅(O₂CPh)₉(MeOH)₃] (2).

EXPERIMENTAL SECTION

Syntheses. All manipulations were carried out under aerobic conditions using chemicals as received, unless otherwise stated. $N^nBu_4MnO_4$ was prepared as described elsewhere. ¹⁷

 $[Ce_3Mn_5O_8(OMe)(O_2CBu^t)_{13}(MeOH)]$ (1). To a stirred orange solution of (NH₄)₂Ce(NO₃)₆ (0.76g, 1.38 mmol) and pivalic acid (2.09 g, 20.5 mmol) in MeOH (7.5 mL) was added solid NnBu₄MnO₄ (0.50 g, 1.38 mmol) in small portions, causing a rapid color change to dark brown. The solution was stirred for a further 10 min, filtered, and the filtrate left undisturbed at ambient temperature for 1 week, during which time brown microcrystals had formed. The latter were collected by filtration, washed with MeOH, dissolved in CH2Cl2, and layered with MeCN (10 mL) to slowly give X-ray quality brown plate-like crystals of $1 \cdot x$ (solv) over 3 days. The sample for crystallography was kept in mother liquor, otherwise the crystals were collected by filtration, washed with MeCN, and dried under vacuum. The yield was 22% based on Mn. Anal. calcd (found) for 1 (solvent-free; $C_{67}H_{124}Ce_3Mn_5O_{36}$): C, 36.56 (36.55); H, 5.68 (5.71); N, 0.00 (0.00) %. Selected IR data (KBr, cm⁻¹): 3362 (w), 3160 (w), 2961 (s), 2929 (m), 2872 (w), 1546 (s), 1483 (s), 1459 (w), 1413 (s), 1377 (s), 1225 (s), 1090 (w), 1028 (m), 939 (w), 899 (m), 786 (m), 618 (s), 587 (m), 562 (m), 543 (m), 500 (m), 449 (m).

 $[Ce_2Mn_3O_5(O_2CPh)_9(MeOH)_3]$ (2). To a stirred orange solution of $(NH_4)_2[Ce(NO_3)_6]$ (0.38 g, 0.69 mmol) and benzoic acid (1.25 g, 10.3 mmol) in MeOH/MeCN (15 mL, 1:1 v/v) was added solid NⁿBu₄MnO₄ (0.25 g, 0.69 mmol) in small portions, causing a rapid color change to dark brown. The solution was stirred for a further 20 min, filtered, and the filtrate left undisturbed at ambient temperature for 4 days, during which time X-ray quality dark red plate-like crystals of 2.xMeCN had formed. The sample for crystallography was maintained in mother liquor, otherwise the crystals were collected by filtration, washed with MeCN, and dried under a vacuum. The yield was 54% based on Mn. Anal. calcd (found) for 2·1/2MeCN·2H2O $(C_{67}H_{62.5}Ce_3Mn_2N_{0.5}O_{28})$: C, 45.52 (45.49); H, 3.56 (3.12); N, 0.40 (0.55) %. Selected IR data (KBr, cm⁻¹): 3383 (wb), 3064 (w), 2836 (w), 2535 (w), 2291 (w), 1970 (w), 1823 (w), 1690 (m), 1599 (s), 1543 (s), 1492 (m), 1391 (sb), 1176 (m), 1070 (w), 1025 (m), 937 (w), 842 (w), 717 (s), 685 (m), 630 (s), 565 (m), 478 (m).

X-ray Crystallography. Data on $1 \cdot x$ (solv), and $2 \cdot x$ MeCN were collected at 100 K on a Bruker DUO diffractometer using Mo K α radiation ($\lambda = 0.71073$ Å) and an APEXII CCD area detector. Raw data frames were read by the SAINT¹⁸ program and integrated using 3D profiling algorithms. The resulting data were reduced to produce hkl reflections and their intensities and estimated standard deviations. The data were corrected for Lorentz and polarization effects and numerical absorption corrections were applied based on indexed and measured faces. The structure was solved using SHELXTL2014 and refined on F^2 using full-matrix least-squares cycles. The non-H atoms were refined with anisotropic thermal parameters, and all the H atoms were placed in calculated, idealized positions and refined as riding on their parent atoms. R_1 is calculated to provide a reference to the conventional R value but its function was not minimized.

For $1 \cdot x$ (solv), the asymmetric unit consists of the whole $\text{Ce}_3 \text{Mn}_5$ cluster, a 30% occupancy $\text{CH}_2 \text{Cl}_2$ solvent molecule, and three $\text{H}_2 \text{O}$

molecules with occupancies of 20%, 20%, and 30%. Ten of the 13 Bu^tCO₂⁻ ligands exhibit disorder in their Me positions; two of the 10 also show disorder in their tertiary C atom. Each disordered group was refined in two parts with their site occupation factors fixed in the final refinement cycles. The H atom attached to the MeOH oxygen atom O9 was calculated in an idealized position. In the final refinement cycle, 22 869 reflections, of which 12 517 are observed with $I > 2\sigma(I)$, were used to refine 996 parameters, and the resulting R_1 , wR_2 , and S (goodness of fit) were 5.71%, 11.66%, and 0.943, respectively.

For $2\cdot x \text{MeCN}$, the asymmetric unit consists of the whole Ce_2Mn_3 cluster and 2.35 MeCN solvent molecules. There are two MeCN molecules in general positions; the N1 molecule has its Me group disordered in two parts, which were refined with site occupation factors of 60:40%. The partial MeCN with 35% occupancy is coupled with the minor component of the MeOH ligand disorder. The methanol Me group and the OH proton were refined in two parts in a 65:35% ratio, and these were fixed in the final refinement cycles. The OH protons of the other two MeOH ligands were obtained from a difference Fourier map and refined freely. In the final cycle of refinement, 16 755 reflections, of which 15 416 are observed with $I > 2\sigma(I)$, were used to refine 951 parameters, and the resulting R_1 , wR_2 , and S were 3.67%, 8.32%, and 1.216, respectively. Crystal data and structure refinement parameters are listed in Table 1.

Table 1. Crystal Data and Structure Refinement Parameters for Complexes 1 and 2

	$1 \cdot x(\text{solv})$	2∙xMeCN
formula ^a	$C_{67}H_{124}Ce_3Mn_5O_{36}$	$C_{66}H_{57}Ce_{2}Mn_{3}O_{26}$
fw, g/mol ^a	2200.77	1711.19
space gp	$P\overline{1}$	$P\overline{1}$
a, Å	14.7686(11)	13.5973(9)
b, Å	15.6052(12)	13.7718(9)
c, Å	24.0557(18)	21.9362(14)
α , deg	94.2826(12)	101.1472(11)
β , deg	99.8132(11)	95.0794(11)
γ, deg	112.6411(11)	113.0642(10)
V, Å ³	4981.6(7)	3646.2(4)
Z	2	2
T, K	100(2)	100(2)
λ, Å ^b	0.71073	0.71073
$ ho_{ m calcd}$ g/cm ³	1.492	1.644
μ , mm ⁻¹	2.042	1.810
$R_1^{c,d}$	0.057	0.0367
wR_2^{e}	0.1357	0.0832

^aExcluding solvent molecules. ^bGraphite monochromator. ^cI > 2σ(I). ^dR₁ = 100Σ(||F_o| - |F_c||)/Σ|F_o|. ^ewR₂ = 100[Σ[w(F_o² - F_c²)²]/Σ[w(F_o²)²]]^{1/2}, w = 1/[σ²(F_o²) + [(ap)² + bp], where $p = [\max(F_o^2, 0) + 2F_c^2]/3$.

High-Field/Frequency EPR (HFEPR) Spectroscopy. HFEPR measurements were performed on complex 1 at the Electron Magnetic Resonance facility of the U.S. National High Magnetic Field Laboratory on a polycrystalline powder sample over a range of frequencies from 120 to 330 GHz and at temperatures in the $5-30~\rm K$ range. The polycrystalline sample was finely ground into powder and tightly pressed into a Teflon cup that was then mounted within the sample chamber of a broadband microwave transmission probe. ¹⁹ The HFEPR probe was subsequently inserted into a variable-flow ⁴He cryostat situated within the bore of a $15/17~\rm T$ superconducting solenoid. Microwaves were generated using a Virginia Diodes Inc. source comprised of a tunable oscillator ($13\pm1~\rm GHz$) followed by a cascade of solid-state multipliers and amplifiers. Field-modulation was employed together with a homodyne lock-in detection scheme using a helium-cooled bolometer, yielding derivative-mode spectra (dI/dB,

where I is the absorption intensity and B the magnetic induction). Spectral simulations were performed using the program EasySpin.²⁰

DFT Methods. Calculations were carried out within the framework of Kohn-Sham density functional theory (DFT)²¹ using the spin-polarized Perdew-Burke-Ernzerhof (PBE) exchange correlation functional²² and projector-augmented wave (PAW)² pseudopotentials in conjunction with the plane-wave basis as implemented in the Vienna Ab-initio Simulation Package (VASP).^{24,25} The plane-wave cutoff energy is 500 eV, and the energy threshold for self-consistency is 10⁻⁵ eV. Owing to the strong localization of the Ce f electrons, the GGA+U method was applied with $U = 2 \text{ eV}^{26}$ for the Ce f orbitals. The downfolding procedure refers to the construction of an effective Hamiltonian that uses basis functions centered only on metal atoms/ions of interest (e.g., Mn) and reproduces the original energy levels (or energy bands in solids) in a given energy range, typically around the HOMO-LUMO gap (or the Fermi energy in a solid). Matrix elements of the effective Hamiltonian are calculated as $\langle W_n | \hat{H} | W_m \rangle$, where \hat{H} is the Hamiltonian and $|W\rangle$ are spatially localized orbitals, or the so-called Wannier functions generated from unitary transformation of Bloch waves.27,2

Other Studies. Infrared spectra in the 400–4000 cm⁻¹ range were recorded on crushed polycrystalline samples as KBr pellets on a Nicolet Nexus 670 FTIR spectrometer. Elemental analyses (C, H, and N) were performed by Atlantic Microlabs, Inc. Variable-temperature dc and ac magnetic susceptibility data were collected on vacuum-dried solids using a Quantum Design MPMS-XL SQUID magnetometer equipped with a 7 T magnet and operating in the 1.8-300 K range. Samples were embedded in solid eicosane in a gel capsule to prevent torqueing. Pascal's constants were used to estimate the diamagnetic corrections, ²⁹ and contributions from the eicosane and gel capsule were measured as a blank. These were subtracted from the experimental susceptibility to give the molar paramagnetic susceptibility $(\chi_{\rm M})$. Magnetization vs field and temperature data were fit using the program MAGNET,³⁰ and D vs g fit error surfaces were generated with the program GRID.³¹ Ac magnetic susceptibility measurements were carried on microcrystalline vacuum-dried samples in the 1.8-15.0 K range using a 3.5 G ac field with oscillation frequencies of 50-

■ RESULTS AND DISCUSSION

Syntheses. The syntheses of 1 and 2 involve the reductive aggregation of $\rm MnO_4^-$ in MeOH in the presence of $\rm (NH_4)_2Ce(NO_3)_6$ and an excess of carboxylic acid. The alcohol is the reducing agent and a potential source of alkoxide ligands, whereas the acid provides carboxylate ligands and ensures an acidic environment that prevents formation of Mn oxide/hydroxide precipitates. After preliminary screening of $\rm MnO_4^-/Ce^{4+}$ reagent ratios, the 1:1 ratio was found to give the highest yields. Complexes 1 and 2 contain only $\rm Mn^{III/IV}$ and $\rm Ce^{IV}$, i.e., no $\rm Mn^{II}$ or $\rm Ce^{III}$.

The 1:1:15 $N^nBu_4MnO_4/(NH_4)_2Ce(NO_3)_6/^tBuCO_2H$ reaction system in MeOH gave a dark brown solution and subsequent isolation of $1 \cdot x(\text{solv})$ containing $3Ce^{IV}$, $2Mn^{III}$, and $3Mn^{IV}$ (eq 1; $R = {}^tBu$). Since previous studies of reductive aggregation of MnO_4^- in homometallic chemistry had

$$5MnO_4^- + 3Ce^{4+} + 13RCO_2H + 2MeOH + 17e^-$$

 $+ 10H^+ \rightarrow [Ce_3Mn_5O_8(OMe)(O_2CR)_{13}(MeOH)]$
 $+ 12H_2O$ (1)

shown the product often to be sensitive to the acid used, ¹⁵ we also explored the reaction with benzoic acid, in MeOH/MeCN to solubilize it, and obtained instead $2 \cdot x$ MeCN (eq 2; R = Ph) containing $2Ce^{IV}$, Mn^{III} , and $2Mn^{IV}$. Notwithstanding their different nuclearities, 1 and 2 are overall

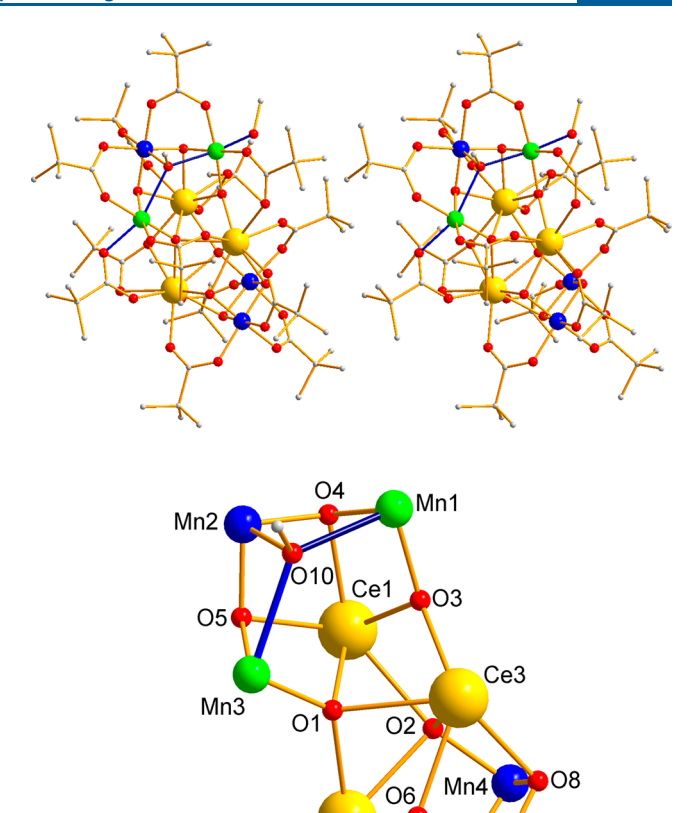


Figure 1. (top) The complete structure of **1** as a stereopair with H atoms omitted for clarity and (bottom) its labeled core. The Mn^{III} Jahn–Teller axes are indicated as blue bonds. Color code: Ce^{IV} , yellow; Mn^{IV} , blue; Mn^{III} , green; O, red; C, gray.

Ce2

$$3MnO_4^- + 2Ce^{4+} + 9RCO_2H + 3MeOH + 10e^- + 5H^+$$

 $\rightarrow [Ce_2Mn_3O_5(O_2CR)_9(MeOH)_3] + 7H_2O$ (2)

similar in that they contain both Ce and Mn with the former always Ce^{IV} and the latter at comparable oxidation state averages of +3.60 (1) and +3.67 (2). In addition, 1 and 2 contain similar subunits, although overall they are structurally different (vide infra).

Description of Structures. Selected metric parameters for 1 and 2 are listed in Tables S1 and S3, respectively, in the Supporting Information. Ce and Mn oxidation states and O protonation levels were confirmed by bond valence sum (BVS) calculations (Tables S2 and S4 of the Supporting Information).³²

Complex 1 contains a $[Ce_3Mn_5(\mu_3-O)_6(\mu_4-O)_2(\mu_3-OMe)]^{13+}$ core (Figure 1) comprising a central Ce^{IV}_3 triangle bridged by four O^2 ions (O1–3 and O6) to which are attached a triangular $\{Mn_3O_2(\mu_3-OMe)\}$ unit at one end and a $\{Mn_2O_2\}$ unit at the other. Alternatively, the core can be described as a $\{Ce^{IV}_2Mn^{IV}_2O_4\}$ cubane attached to a $\{Ce^{IV}Mn^{IV}_2Mn^{III}O_3(OMe)\}$ deformed cubane opened up at one face by insertion of an additional O^2 ion (O1 or O3). The Jahn–Teller (JT) elongation axes of the two Mn^{III} atoms Mn1 and Mn3 meet at the MeO^- oxygen atom O10. Peripheral ligation is completed by 13 pivalate groups, 11 in the common syn,syn $\eta^1:\eta^1:\mu$ bridging mode, one in the $\eta^1:\eta^2:\mu_2$ mode, and one in a chelating (η^2) mode which is also

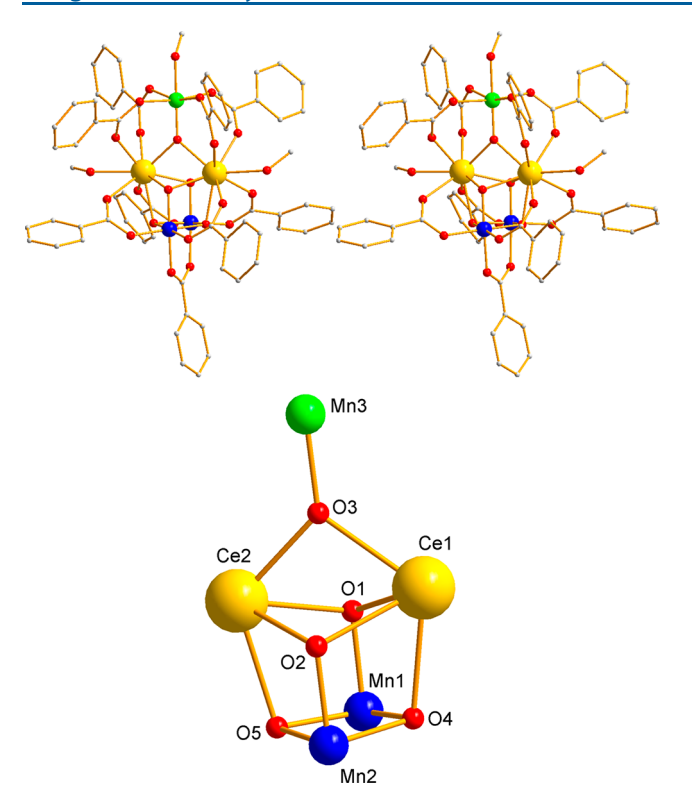


Figure 2. (top) The structure of **2** as a stereopair with H atoms omitted for clarity and (bottom) its labeled core. Color code: Ce^{IV}, yellow; Mn^{IV}, blue; Mn^{III}, green; O, red; C, gray.

hydrogen-bonded to a terminal MeOH on Mn3 (O9···O12 = 2.769(8) Å). There are no significant contacts between neighboring molecules of 1. The core of 1 is similar to that in $[Ce_3Mn_5O_9(O_2CBu^t)_{12}(NO_3)(C_4H_4O)]^{,33}$ but the latter is at a different oxidation level of $Mn^{IV}_4Mn^{III}$ and has a μ -O²⁻ at the μ_3 -MeO⁻ position.

Complex 2 contains a $[Ce_2Mn_3(\mu_3-O)_5)]^{9+}$ core (Figure 2) comprising a $\{Ce^{IV}_2Mn^{IV}_2(\mu_3-O)_4\}$ cubane with a Mn^{III} bridged to the Ce^{IV} atoms by an additional O^{2-} ion, O3. Peripheral ligation is completed by three terminal MeOH ligands on Ce1, Ce2, and Mn3 and nine $\eta^1:\eta^1:\mu_2$ bridging benzoate groups. The molecule has virtual $C_{2\nu}$ symmetry, ignoring the orientation of benzoate Ph rings and alcohol Me groups. The expected Mn^{III} JT distortion at Mn3 is of the rarer axial compression type rather than the common axial elongation: (i) the Mn-O²⁻ bond (Mn3-O3 = 1.803(5) Å) is 0.05-0.10 Å shorter than typical $Mn^{III}-(\mu_3-O^{2-})$ bonds (e.g., Mn1-O4 = 1.882(8) Å and Mn3-O5 = 1.891(8) Å in 1), and (ii) the Mn^{III}-O(carb) bonds (2.043(3)-2.090(3) Å) are slightly longer than those in 1 (1.915(3) and 1.940(3) Å). Both observations are consistent with a JT compression axis. Unlike 1, 2 also has intermolecular contacts involving the benzoate rings, the most significant being $\pi - \pi$ stacking (3.49) Å) involving Ph rings of benzoates bridging Ce1Mn3 pairs on adjacent molecules (Figure S3 of Supporting Information). 2 has been previously obtained from a different synthetic procedure involving oxidation of Mn(O2CPh)2 with $(NH_4)_2Ce(NO_3)_6$ in $MeOH/MeCN.^{34}$

A comparison of the cores of 1 and 2 shows that the latter is a fragment of the former (the $\{Ce_2Mn_2O_4\}$ cubane plus atoms O1 and Mn3), and this provides some qualitative insight into how the identity of the employed carboxylate is affecting the synthetic pathway involving aggregation of the complete core

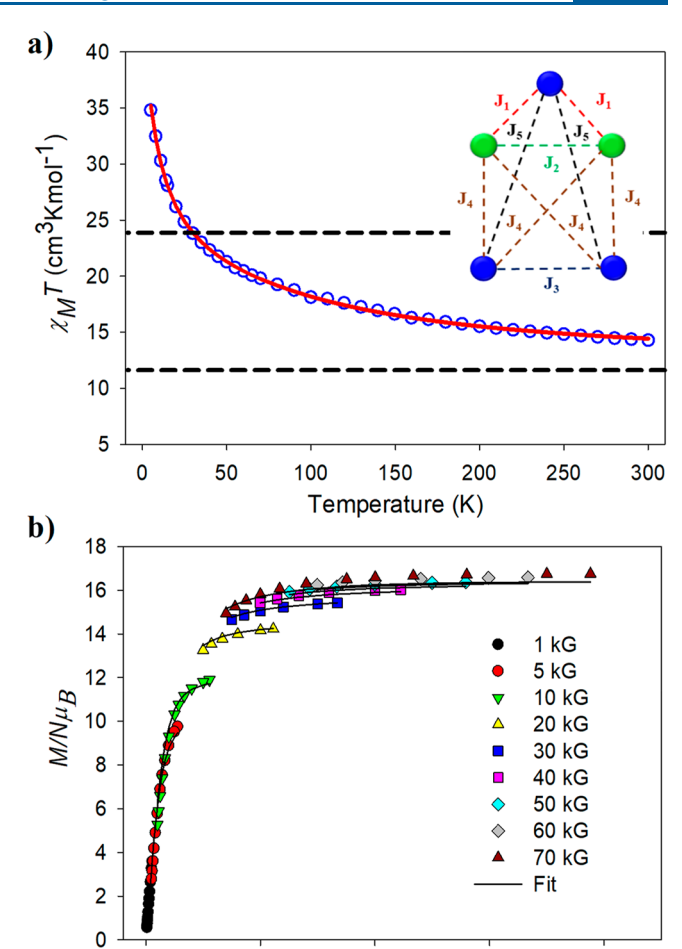


Figure 3. (a) $\chi_{\rm M}T$ vs T for complex 1 in a 1.0 kG dc field. The lower and upper dashed lines are spin-only values for, respectively, (i) five noninteracting ${\rm Mn^{IV}}_3{\rm Mn^{III}}_2$ ions and (ii) noninteracting ${\rm Mn^{IV}}_2$ (S=3) and ${\rm Mn^{IV}}_3{\rm Mn^{III}}_2$ ($S=1^{11}/_2$) units. The solid line is the fit to the exchange-coupling model in the inset (${\rm Mn^{III}}$, green; ${\rm Mn^{IV}}$, blue). See the text for the fit parameters. (b) $M/N\mu_{\rm B}$ vs H/T plot for data in the 1.8–10.0 K range at the indicated applied fields. The solid line is the fit; see the text for the fitting model and the fit parameters.

20

H/T(kG/K)

30

40

10

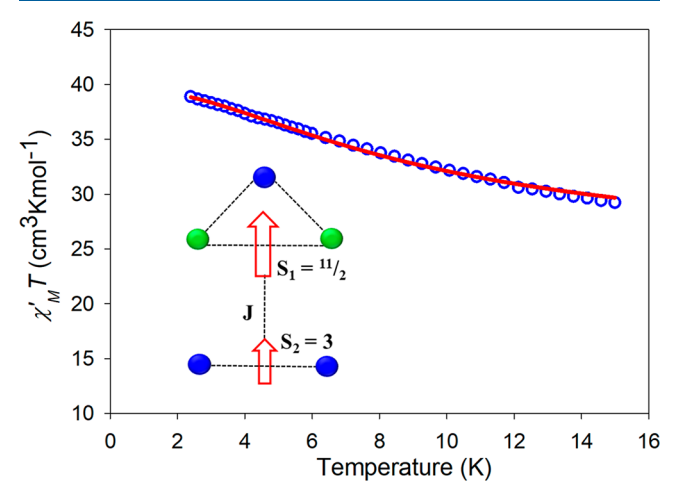
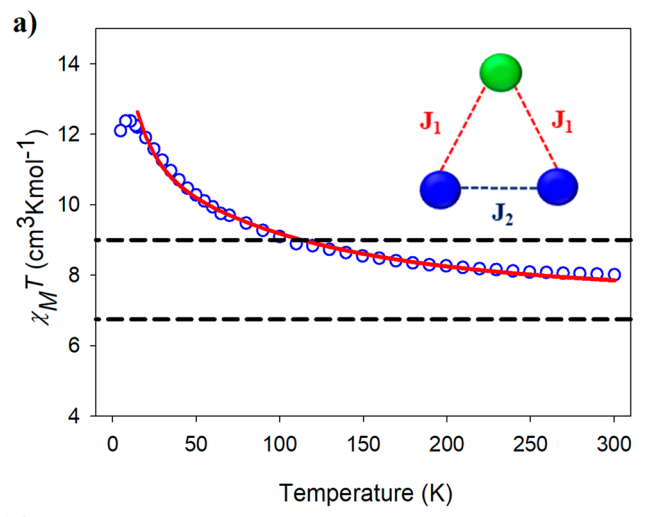


Figure 4. Ac in-phase $\chi_{\rm M}{}'T$ vs T for complex 1 in a 3.5 G ac field at 1000 Hz. The solid line is the fit using the Van Vleck equation to the two-spin model in the inset. See the text for the fit parameters.



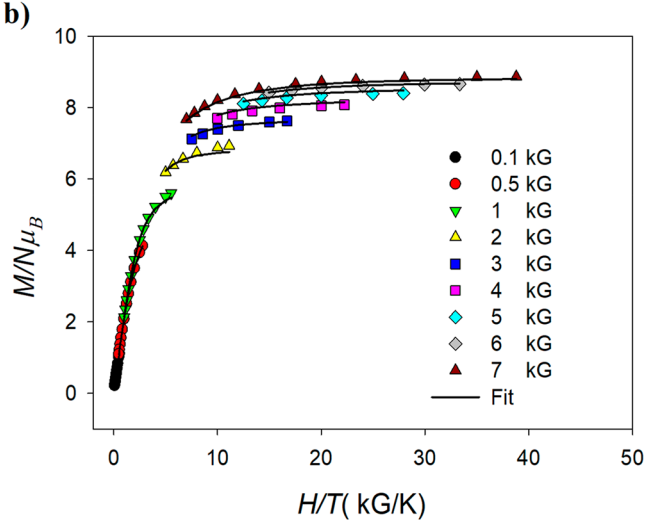


Figure 5. (a) $\chi_{\rm M}T$ vs T for ${\bf 2}$ in a 1.0 kG dc field. The lower and upper dashed lines are spin-only values for, respectively, (i) three noninteracting ${\rm Mn^{IV}}_2{\rm Mn^{III}}$ ions and (ii) noninteracting ${\rm Mn^{IV}}_2$ (S=3) and ${\rm Mn^{III}}$ (S=2) units. The solid line is the fit to the Van Vleck model in the inset (${\rm Mn^{III}}$, green; ${\rm Mn^{IV}}$, blue); see the text for the fit parameters. (b) $M/N\mu_{\rm B}$ vs H/T plot for ${\bf 2}$ in the 1.8–10.0 K range at the indicated applied fields. The solid line is the fit; see the text for the fitting model and the fit parameters.

of 1, i.e., the benzoate groups appear to be stabilizing the smaller $[Ce_2Mn_3O_5]$ core and preventing its further growth.

Magnetochemistry: DC Magnetic Susceptibility Studies. Variable-temperature dc magnetic susceptibility $(\chi_{\rm M})$ data were collected on crushed vacuum-dried microcrystalline samples in the 5.0–300 K range in a 0.1 T (1 kG) applied dc field and plotted as $\chi_{\rm M} T$ vs T.

For 1, $\chi_{\rm M}T$ steadily increases from 14.27 cm³ K mol⁻¹ at 300 K to 34.79 cm³ K mol⁻¹ at 5.0 K (Figure 3a). The 300 K value is higher than the spin-only $(g=2.0)~\chi_{\rm M}T=11.63~{\rm cm}^3$ K mol⁻¹ for a noninteracting Mn^{IV}₃Mn^{III}₂ system, indicating dominant ferromagnetic (F) interactions in 1. However, F Mn^{III}₂Mn^{IV} and Mn^{IV}₂ units with $S=^{11}/_2$ and S=3, respectively, that are well-separated and essentially noninteracting would give a maximum spin-only $\chi_{\rm M}T$ of 23.88 cm³ K mol⁻¹ at low T (with a likely decrease at even lower T as any very weak interunit antiferromagnetic (AF) interactions became evident). Instead, a much higher $\chi_{\rm M}T$ of 34.79 cm³ K mol⁻¹ at 5.0 K is obtained, suggesting the presence of long-

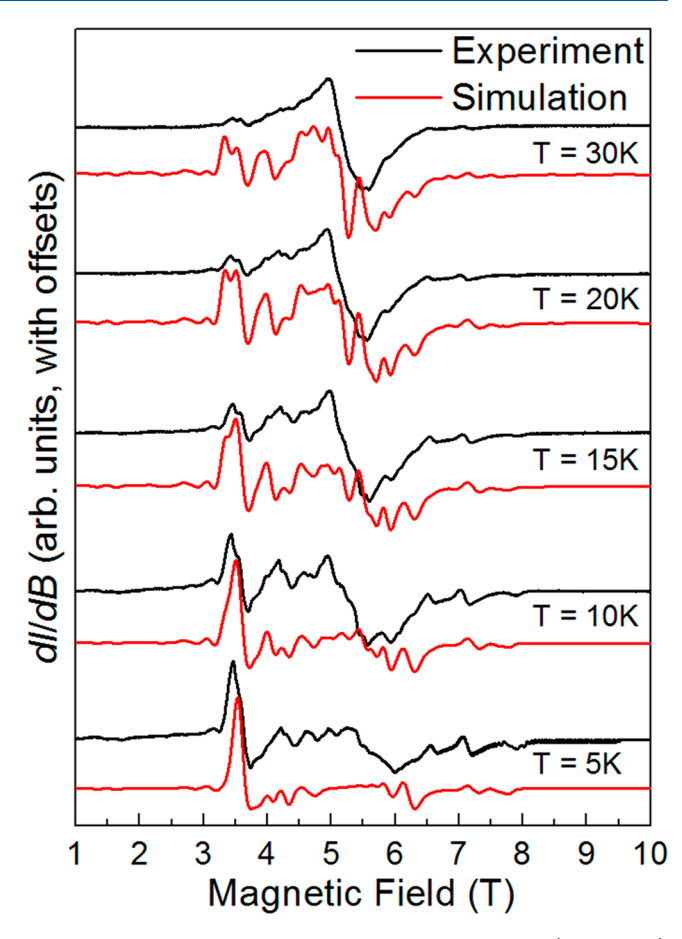


Figure 6. Variable-temperature powder HFEPR spectra (black lines) recorded at a frequency of 144 GHz, along with spectral simulations (red lines) generated using eq 6 along with the parameters given in the main text. See also Figure S6 in the Supporting Information for frequency dependent measurements and simulations.

range F interactions of significant magnitude between the two units. This predicts an $S = {}^{17}/{}_2$ ground state, the maximum possible (spin-only $\chi_{\rm M}T = 40.38~{\rm cm}^3~{\rm K~mol}^{-1}$), which is consistent with the still-increasing value at 5.0 K.

Confirmation of the ground state of 1 came from magnetization (M) vs field (H) and T data in the 0.1–7.0 T and 1.8–10.0 K ranges, respectively. The data, as reduced magnetization ($M/N\mu_{\rm B}$) vs H/T (Figure 3b), where N is Avogadro's number and $\mu_{\rm B}$ is the Bohr magneton, were fit by diagonalization of the spin Hamiltonian matrix using the program MAGNET, which assumes that only the ground state is occupied, includes the axial zero-field splitting $(D\hat{S}_z^2)$ and the Zeeman interaction, and incorporates a full powder average. The corresponding spin Hamiltonian is eq 3

$$\hat{H} = D\hat{S}_z^2 + g\mu_B \mu_0 \hat{S} \cdot \mathbf{H} \tag{3}$$

where \hat{S}_z is the *z*-axis spin operator, *g* is the Landé *g* factor, and μ_0 is the vacuum permeability. An excellent fit (solid lines in Figure 3b) employing all data was obtained with $S = {}^{17}/_2$, g = 1.95(3), and D = -0.14(1) cm⁻¹. The *D* vs *g* error surface (Figure S1 of Supporting Information) revealed a best-fit minimum rather soft in *g* giving the quoted uncertainties in the fit parameters. Also, as is usually the case, a second fit with positive *D* was also observed, but of poorer overall quality.

To avoid any possible complications from the dc field, ac inphase susceptibility (χ_{M}') data were collected. The $\chi_{M}'T$ vs T

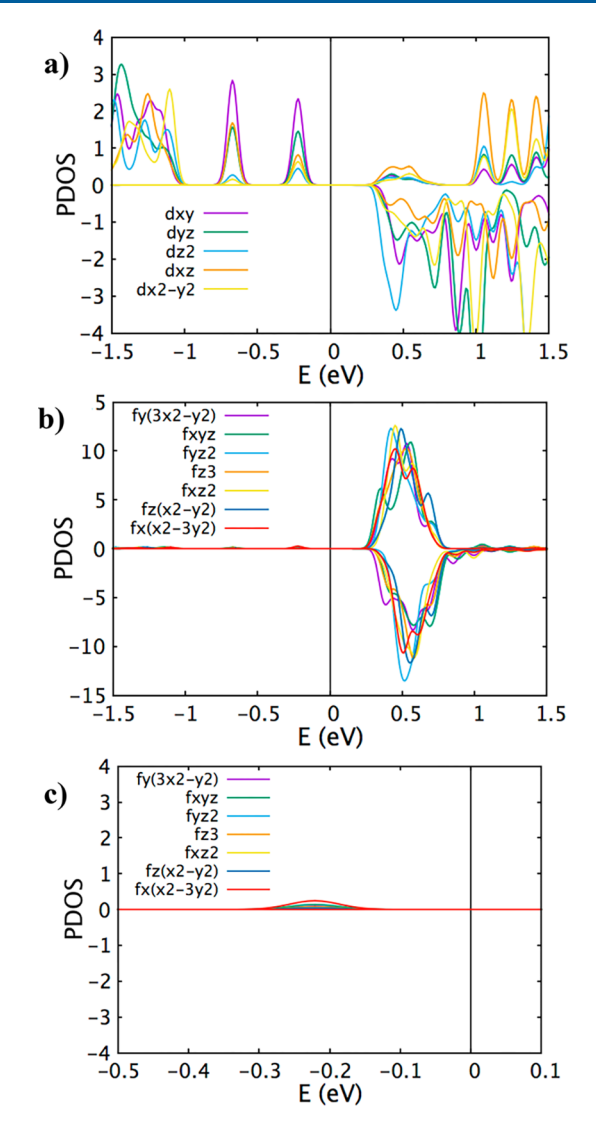


Figure 7. Projected density of states (PDOS) of (a) the Mn-d and (b) the Ce-f orbitals of complex 1 and (c) an expansion of the small Ce contribution at \sim -0.2 eV.

plot (Figure S2) increases steadily with decreasing T from 29.20 cm³ K mol⁻¹ at 15.0 K to a plateau of 38.8 cm³ K mol⁻¹ at 2.4 K, providing further confirmation of an $S = {}^{17}/{}_2$ ground state with $g \sim 1.96$. Below 2.4 K, there is a barely discernible decrease at 1000 Hz assigned to slow relaxation of the magnetization vector, confirmed by a very weak and frequency-dependent out-of-phase $(\chi_{\rm M}{}'')$ signal (Figure S2) showing that 1 is a new SMM but a very poor one.

The dc $\chi_{\rm M}T$ data for 1 (Figure 3a) were fit using the program PHI³⁵ to determine the various exchange couplings (J_{ij}) , using the $-2J_{ij}\hat{S}_i\hat{S}_j$ convention) as defined in Figure 3 (inset). To minimize overparameterization, virtual symmetry was applied: $J_1 = J({\rm Mn^{III}Mn^{IV}})$, $J_2 = J({\rm Mn^{III}Mn^{III}})$ in the triangular unit, J_3 (${\rm Mn^{IV}Mn^{IV}}$) in the Mn^{IV} pair, and $J_4 = J({\rm Mn^{III}Mn^{IV}})$ and $J_5 = J({\rm Mn^{IIV}Mn^{IV}})$ for the long-range interactions. An excellent fit (solid line in Figure 3a) was obtained with $J_1 = +11.36(2)$ cm⁻¹, $J_2 = -2.02(7)$ cm⁻¹, $J_3 = +26.2(1.4)$ cm⁻¹, $J_4 = +0.26(1)$ cm⁻¹, and $J_5 = +0.026(12)$ cm⁻¹, with g and temperature-independent paramagnetism (TIP) held constant at 2.0 and 800×10^{-6} cm³ mol⁻¹, respectively. The strongest interactions, J_1 and J_3 , are thus both

F and can be rationalized as resulting from the acute Mn–O–Mn angles of average 97.3° and 95.5° between the Mn^{III}Mn^{IV} and Mn^{IV}Mn^{IV} pairs, respectively. This is also consistent with previous observations of F interactions between Mn^{IV}Mn^{IV} pairs in cubane-like units with bridging Mn–O–Mn angles of ~97° or less. ³⁶ The F J_3 gives an S=3 ground state for the Mn^{IV}Mn^{IV} pair, whereas within the triangular Mn₃ unit there is spin frustration involving F J_1 and AF J_2 . The stronger J_1 clearly dominates, leading to an $S={}^{11}/{}_2$ ground state for this unit. The ground state of the whole cluster is then determined by the long-range J_4 and J_5 , mainly the stronger former, which are both F and thus rationalize the experimental $S={}^{17}/{}_2$ ground state.

However, we worried that since the strong J_1-J_3 dominate the spin state energy manifold and resulting Boltzmann populations, the obtained I_4 value (and I_5) was very unreliable. We therefore determined independently the interaction between the two Mn units by fitting the ac $\chi_{\text{M}}T$ vs T data below 15 K to the Van Vleck equation for a two-spin system, S_1 = $^{11}/_{2}$ and S_{2} = 3, interacting with exchange constant J (Figure 4, inset). This model assumes both units are in their local ground states, which is reasonable given the low T and the strength of J_1 and J_3 , and the use of ac $\chi_M{}'T$ vs T data also avoids possible complications from the use of an applied dc field given how weak the interactions of interest are. Using data down only to 2.4 K (to avoid the effect of slow relaxation below this), a satisfactory fit was obtained (solid line in Figure 4) with J = +0.26(1) cm⁻¹ and g = 1.98(1). Thus, J from this independent approach is (coincidentally) identical to J_4 from the fit of dc data, supporting the magnitude of the long-range

For 2, $\chi_{\rm M}T$ steadily increases from 8.00 cm³ K mol⁻¹ at 300 K to 12.37 cm³ K mol⁻¹ at 10.0 K and then decreases slightly to 12.09 cm³ K mol⁻¹ at 5.0 K (Figure 5). The 300.0 K value is higher than the spin-only 6.75 cm³ K mol⁻¹ for noninteracting Mn^{IV}₂Mn^{III} ions, indicating F interactions between the two Mn^{IV}'s. As for 1, the maximum at 10.0 K is higher than the 9.00 cm³ K mol⁻¹ spin-only value for noninteracting Mn^{IV}₂ (S = 3) and Mn^{III} (S = 2) units, indicating the presence again of long-range F interactions between the two units and thus an S = 5 ground state for 2 (spin-only $\chi_{\rm M}T$ = 15.0 cm³ K mol⁻¹). However, we expected the $\chi_{\rm M}T$ to peak closer to this value and thus suspected and found $\pi-\pi$ interactions involving benzoate Ph rings 3.49 Å apart on adjacent molecules (Figure S3); i.e., the $\chi_{\rm M}T$ stops increasing as very weak AF intermolecular interactions through the $\pi-\pi$ contacts become evident.

The data were fit to the $\chi_{\rm M}T$ vs T Van Vleck equation³⁷ for an isosceles triangle (Figure 5a inset) with the spin Hamiltonian of eq 4, where $J_1 = J({\rm Mn^{II}Mn^{IV}})$, $J_2 = J({\rm Mn^{IV}Mn^{IV}})$, $S_1 = 2$, and $S_2 = S_3 = \frac{3}{2}$. Use of the Kambe vector coupling scheme³⁸ with $\hat{S}_{\rm A} = \hat{S}_2 + \hat{S}_3$ and $\hat{S}_{\rm T} = \hat{S}_{\rm A} + \hat{S}_1$, where $S_{\rm T}$ is the total spin of the molecule

$$\hat{H} = -2J_1[\hat{S}_1 \cdot \hat{S}_2 + \hat{S}_1 \cdot \hat{S}_3] - 2J_2\hat{S}_2 \cdot \hat{S}_3$$
(4)

$$E(S_{\rm T}, S_{\rm A}) = -J_1[(S_{\rm T}(S_{\rm T}+1) - S_{\rm A}(S_{\rm A}+1)] - J_2S_{\rm A}(S_{\rm A}+1)$$
(5)

leads to the energies of the resultant spin states, $E(S_{\rm T}, S_{\rm A})$, given by the eigenvalue expression of eq 5. The fit (solid line in Figure 5a) gave $J_1 = +1.0(1)$ cm⁻¹, $J_2 = +20.8(4)$ cm⁻¹, and g = 1.99(3). This fit indicates an S = 5 ground state, the $|S_{\rm T}, S_{\rm A}\rangle = |5,3\rangle$ state, with a $|4,3\rangle$ first excited state at 10.1 cm⁻¹ higher

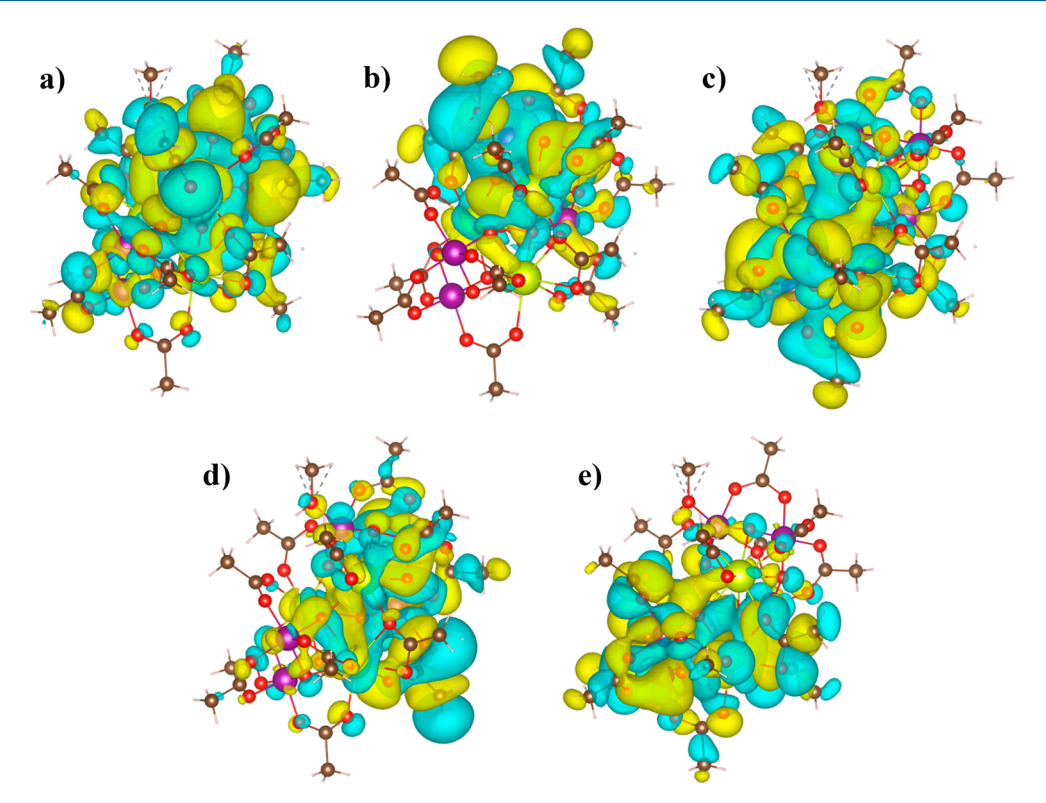


Figure 8. Wannier functions projected onto Mn- d_{xy} orbitals for complex 1. The first Wannier orbital has the largest spread of 6.96 Å². The isosurface value is $1.5/\sqrt{V}$, where V is the unit cell volume.

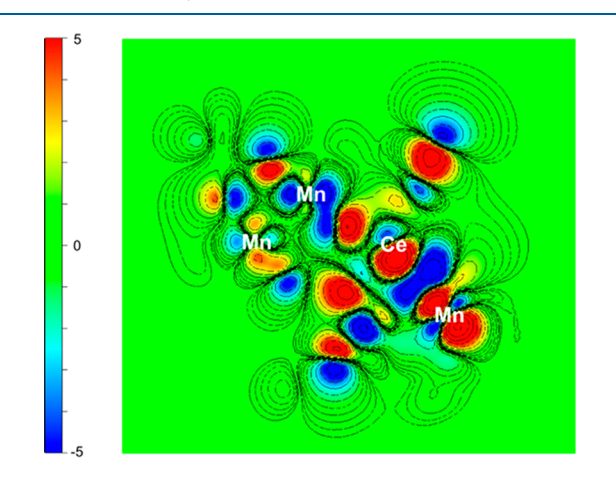


Figure 9. Cross-sectional contour plot, in units of $0.00827 \text{ Å}^{-3/2}$, of a plane through the Mn2, Mn4, and Mn5 ions in the Wannier function of Figure 8a for 1.

energy. The data were also fit using the program PHI to the same isosceles triangle model to give an essentially identical fit, with $J_1 = +0.95(24)$ cm⁻¹, $J_2 = +19.4(6)$ cm⁻¹, and a fixed g = 2.0 (Figure S4). A good fit of $M/N\mu_B$ vs H/T data collected in fields up to 7 T was also obtained (Figure Sb), with S = 5, D = -0.40(3) cm⁻¹, and g = 1.82(2). The low value of g is an artifact assigned to the effect of the intermolecular interaction, and the D value should also be considered very approximate, but otherwise the fit confirms the long-range F coupling to give an overall S = 5 ground state. The D vs g fit error surface is shown in Figure S5. Thus, both 1 and 2 exhibit significant long-range F interactions between the two Mn-containing units separated by four bonds via diamagnetic Ce^{IV} ions, rather than

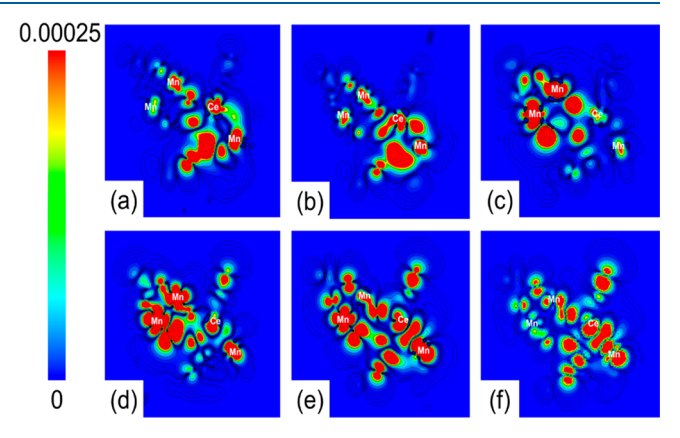


Figure 10. (a—e) Cross-sectional contour plots of the charge density of the five highest occupied KS states for 1, in units of Bohr⁻³. The maximum and minimum (0.00025 and 0) of the scale are set to match the maximum and minimum values of the states. Energies are from high to low, within 1 eV of each other. (f) For comparison a plot is shown of one of the Wannier orbitals.

the very weak AF ones that would usually be predicted in such cases.

High-Frequency/Field EPR (HFEPR) Studies. Figure 6 shows the experimental variable-temperature HFEPR spectra of 1 recorded at a frequency of 144 GHz, while variable-frequency measurements are presented in Figure S6 of the Supporting Information; also included in both figures are the best simulations generated according to the multispin Hamiltonian given by eq 6, 20,39,40 where the

$$\hat{H}_{\text{MS}} = \sum_{i=1}^{N} \hat{s}_{i} \cdot \vec{d}_{i} \cdot \hat{s}_{i} + \sum_{i} \mu_{\text{B}} \vec{B} \cdot \vec{g}_{i} \cdot \hat{s}_{i} + \sum_{j>i} -2J_{ij} \hat{s}_{i} \cdot \hat{s}_{j}$$

$$\tag{6}$$

first summation describes the local zero-field-splitting (ZFS) at each spin site i in the molecule, N is the total number of spins (N=5 for 1), \hat{s}_i is the associated total spin operator, and d_i is the corresponding traceless symmetric second-rank ZFS tensor (eq 7), with d_i and e_i representing the second-order axial and rhombic ZFS parameters, respectively. Lower-case symbols are used here to differentiate local operators/parameters associated with the individual Mn spins from the macro-spin operators/parameters associated with the coupled molecule.

$$\vec{d}_{i} = \begin{pmatrix} -\frac{d_{i}}{3} + e_{i} & 0 & 0\\ 0 & -\frac{d_{i}}{3} - e_{i} & 0\\ 0 & 0 & \frac{2d_{i}}{3} \end{pmatrix}$$

$$(7)$$

The second summation in eq 6 represents the Zeeman interaction at each site in terms of the individual Landé tensors, \vec{g}_i , and the applied magnetic field, \vec{B} , with μ_B denoting the Bohr magneton. Last, the final double summation in eq 6 describes the isotropic Heisenberg exchange coupling between spin sites i and j within the molecule, parametrized by the scalar coupling constant J_{ii} (using the $-2J_{ii}$ $\hat{s}_i \cdot \hat{s}_i$ convention).

A full treatment considering all five independent Mn spins within 1 involves far too many adjustable parameters and is both computationally demanding and time-consuming when performing orientational averaging for simulations of powder HFEPR spectra. Therefore, we adopted the same model considered in the analysis of the magnetic data to greatly simplify our treatment of the HFEPR measurements and to allow direct comparisons between the various methods employed in this investigation. In this model, the two Mn^{III} ions (Mn1 and Mn3, see Figure 1) at one end of the molecule are considered to be coupled ferromagnetically to the neighboring Mn^{IV} ion (Mn2), giving rise to an effective total spin $s_1 = {}^{11}/{}_2$ (= 2 + 2 + ${}^{3}/{}_2$) at the lowest temperatures. Meanwhile, we assume that the remaining Mn^{IV} ions (Mn4 and Mn5) at the other end of the molecule also couple ferromagnetically, giving rise to a second effective spin $s_2 = 3$ $(= \frac{3}{2} + \frac{3}{2})$. Within this model, we assume that any anisotropy associated with the Mn^{IV} ions is weak in comparison to the JT-active Mn^{III} ions.⁴¹ Hence, we assume that the d_1 tensor dominates the ZFS; i.e., we adjust d_1 and e_1 to reproduce the larger splittings observed in the experimental spectra. Meanwhile, we assume a small axial d_2 tensor, with e_2 = 0 and d_2 ($\ll d_1$) adjusted to improve some of the finer details near the center of the spectra. A final simplification involves assuming the two \vec{g} tensors to be isotropic, with $g_{1\parallel} = g_{2\parallel} = g_{1\perp}$ = $g_{2\perp}$ = 2.00. Although Landé factors slightly less than 2.00 are known for Mn^{III} and Mn^{IV} (literature values span a considerable range, yet high-resolution EPR studies for Mn^{III}/Mn^{IV} generally obtain values between 1.98 and 2.00),⁴² the error introduced by this approximation in terms of estimating the coupling and ZFS parameters is insignificant in comparison to the overall validity of the model. In this way, we are left with just four adjustable parameters, d_1 , e_1 , d_2 , and J_{12} (equivalent to J in the inset to Figure 4).

The simulations presented in Figures 6 and S6 (see Supporting Information) represent best attempts at describing the complete HFEPR data set. We focus primarily on the lowest temperature measurements, as our simple model can be

expected to break down at elevated temperatures, i.e., when the treatment of the two halves of the molecule as effective giant spins starts to fail. 43,44 The following parameters are deduced from this analysis: $J_{12} = +0.20(2) \text{ cm}^{-1}$, $d_1 = -0.40(2) \text{ cm}^{-1}$, e_1 = +0.063(5) cm⁻¹, and d_2 = 0.016(4) cm⁻¹. The first point to note is the F coupling constant, J_{12} , which is in good agreement with the value of J = +0.26(1) cm⁻¹ obtained from the analysis of ac susceptibility data using the same model. Given the degree of approximation employed here, and the obvious fact that the variable-temperature susceptibility analysis ignores the appreciable ZFS within the molecule, one should not expect perfect agreement. Nevertheless, the combined experimental investigations paint a unified picture of the weak F coupling through the diamagnetic Ce^{IV} centers. We note that the HFEPR simulations are quite sensitive to both the magnitude and sign of J_{12} in this weak coupling regime $(J_{12} < d_1)^{.45}$ Hence, we have good confidence in the value reported here. It is also important to rule out a simple through-space dipolar interaction as the source of this coupling. A very simple estimate treating the two halves of the molecule as point dipoles $s_1 = {}^{11}/{}_2$ and $s_2 = 3$, separated by 6 Å, yields a coupling strength that is a factor of ~25 smaller than the experimentally obtained one. Thus, even though this represents a rather crude estimate, it gives us confidence that the observed F interaction is indeed due to exchange through the diamagnetic Ce^{IV} ions.

Meanwhile, one can make a crude estimate of the axial D parameter associated with the $S=^{17}/_2$ ferromagnetically coupled ground state of the complete $\mathrm{Mn_5Ce_3}$ cluster based on the assumption that the dominant contribution comes from the $\mathrm{Mn^{III}}$ ions, i.e., d_1 . Upon doing so, we obtain a value of D=-0.16(2) cm⁻¹ for the $S=^{17}/_2$ ground state of 1, again in good agreement with the value of D=-0.14(2) cm⁻¹ deduced from reduced magnetization measurements, given the approximations employed in both analyses.

DFT Calculations. In previous work with a Ce₃Mn₈ cluster with a very different structural topology, analysis of the magnetic properties led us to suspect that a Ce^{IV} ion was contributing to the exchange coupling between Mn^{III}··Mn^{III} pairs bridged by O²⁻ and/or RCO₂⁻ groups.⁴⁷ Thus, the above results for **1** and **2** now made us wonder whether a similar effect was operative in these clusters with more separated Mn_x units <u>not</u> directly bridged by any ligands. If so, then this would be a much clearer indication of the ability of diamagnetic Ce^{IV} to contribute to Mn^{III}··Mn^{III} exchange couplings.

Calculations were therefore carried out to elucidate the possible involvement of empty Ce^{IV} f orbitals in the long-range exchange coupling. We began with total energy calculations of the 16 spin configurations at the five Mn atoms with a reasonable U = 4.4 eV and found the all-parallel (uuuuu) state (u = up) with $S = {}^{17}/{}_2$ to be the ground state (Table S5), in agreement with the experimental magnetic susceptibility and HFEPR conclusions. The first excited state at just a few millielectronvolts was found to be the (ddduu) state with S = $^{5}/_{2}$, corresponding to the spins of the Mn₃ and Mn₂ units being antiparallel and thus supporting the long-distance interaction between Mn_x units to be the weakest in the molecule. However, the excited state energies were found to be very sensitive to the calculational parameters such as U, precluding subsequent reliable calculation of the various J_{ii} parameters for comparison with those from the experimental magnetic susceptibility fits and HFEPR simulation.

Next, the projected density of states (PDOS) of Mn-d and Ce-f orbitals for 1 (Figures 7a,b) show that the Mn-d_{xy} orbitals

have the largest contribution below the Fermi energy while the contribution from the Ce-f orbitals is mainly above but close to the Fermi energy. This is consistent with the Mn-d orbitals obviously dominating the exchange coupling in the molecule. However, small features for Ce-f orbitals are also seen below the Fermi energy at the positions of Mn-d orbitals, indicating d/f orbital hybridization, with the largest Ce contribution being in the highest energy Mn-d band at ~−0.2 eV (Figure 7c). To further probe this d/f hybridization, the maximally localized Wannier function method²⁸ was employed to assess the spread of the hybridization and its contribution to longrange magnetic interaction pathways. 47 With Wannier functions projected onto the five Mn- d_{xv} orbitals, five Wannier functions were obtained for 1 (Figure 8). The huge spread of 6.96 Å² for the first Wannier orbital (Figure 8a) shows that it is delocalized over the whole molecule, providing a pathway for the long-range interaction between the distant Mn ions in 1. This is better visualized in the slice through this Wannier orbital shown in Figure 9, which emphasizes that it encompasses both distant Mn ions as well as Ce ions.

The same conclusion results from looking at the five highest occupied Kohn-Sham (KS) orbitals, ψ_i (i = 1-5). From the DOS analysis, their major composition is Mn-d orbitals with slight Ce-f hybridization. The partial density (defined as $|\psi_i|^2$) cross-sectional areas are depicted in Figure 10a-e. It can be seen that some of these orbitals are quite diffuse, supporting a significant exchange interaction between distant Mn atoms. For comparison, we also plot one of the Wannier orbitals (Figure 10f). This long-distance interaction is consistent with the effective Hamiltonian approach. The purpose of constructing Wannier orbitals is to reduce the Hilbert space to a few states near the highest occupied molecular state. These states are more important than those of lower energy for superexchange processes. Upon completion of the Wannier transformation, an effective tight-binding Hamiltonian is produced whose off-diagonal elements are related to the hopping process from one site to another. Here, a site is chosen to be a Mn atom. The influence of other atoms such as O and Ce are all included implicitly through this exercise. Unlike total energy calculations, the effective Hamiltonian does not provide the sign of the exchange couplings, but it shows the relative strength of various spin coupling pathways. Our analysis indicates that distant Mn atoms couple together more weakly than neighboring ones, but still within the same order of magnitude (\sim 9:1).

Similar results were obtained for complex **2**, with the generated PDOS plots (Figure S7) showing that now the Mnd z^2 orbitals have the largest contributions below the Fermi energy. In addition, small features for Ce-f orbitals are again seen below the Fermi energy at the positions of Mn-d orbitals, indicating d/f orbital hybridization. Wannier functions projected onto the three Mn-d z^2 orbitals gave the three Wannier functions for **2** in Figure S8, with the one with the largest spread of 4.37 Å 2 being delocalized over the whole molecule and providing a pathway for the long-range interaction between Mn, as visualized in the slice through this Wannier orbital in Figure S9.

CONCLUSIONS

The reductive aggregation of MnO_4^- in heterometallic cluster chemistry for the first time has yielded a new Ce_3Mn_5 cluster (1) and a lower nuclearity Ce_2Mn_3 cluster (2), both exhibiting long-range exchange coupling between Mn ions. These

interactions between well-separated Mn units, indicated by both fits of magnetic susceptibility and HFEPR data, are surprising in both their F nature and their significant magnitude (albeit still weak), given that in both complexes the shortest interunit Mn···Mn separations are ~6 Å and a standard superexchange pathway would involve four bonds through the intervening diamagnetic O²⁻ and Ce⁴⁺ ions. We would have instead predicted very weak AF interactions akin to commonly observed intermolecular interactions between adjacent magnetic molecules in a solid. The possibility that the F interactions instead are due to involvement of empty Ce^{IV} f orbitals is supported by the DFT calculations revealing d/f orbital mixing. In effect, the data indicate that the longrange coupling is mediated by MnCe^{IV}Mn superexchange pathways involving empty Ce^{IV} 4f orbitals. It is not clear at the present time why this leads to F rather than AF coupling in 1 and 2, and this point will need to be addressed both experimentally and theoretically in future work. In fact, we also see no reason why in some compounds it might not be found to be AF, in which case depending on the topology it might not be so easy to distinguish it from weak AF interactions through normal superexchange pathways involving just oxo and/or other O-based ligands. Related work is in progress.

Since the d/f orbital hybridization is a consequence of the Ce-f orbitals being relatively low-lying to the Fermi energy, it is therefore a direct consequence of the high Ce^{IV} oxidation state. We see no reason therefore why similar effects would not be seen in other $3d/Ce^{IV}$ clusters or solid-state materials that have an appropriate topology so that this effect is not masked by stronger couplings—the advantage of the present complexes 1 and 2 was that their component Mn_x units are essentially on opposite sides of the central Ce_x units and thus not directly bridged and coupled with a significant magnitude.

ASSOCIATED CONTENT

Supporting Information

The Supporting Information is available free of charge at https://pubs.acs.org/doi/10.1021/acs.inorgchem.0c00332.

Tables of selected bond distances and angles, bond valence sums, magnetic data (reduced magnetization plots and error surfaces), HFEPR data and PDOS plots for 1 and 2 (PDF)

Accession Codes

CCDC 1975729–1975730 contain the supplementary crystallographic data for this paper. These data can be obtained free of charge via www.ccdc.cam.ac.uk/data_request/cif, or by emailing data_request@ccdc.cam.ac.uk, or by contacting The Cambridge Crystallographic Data Centre, 12 Union Road, Cambridge CB2 1EZ, UK; fax: +44 1223 336033.

AUTHOR INFORMATION

Corresponding Author

George Christou — Department of Chemistry, University of Florida, Gainesville, Florida 32611, United States;
orcid.org/0000-0001-5923-5523; Email: christou@chem.ufl.edu

Authors

Sayak Das Gupta — Department of Chemistry, University of Florida, Gainesville, Florida 32611, United States

Robert L. Stewart — National High Magnetic Field Laboratory and Department of Physics, Florida State University, Tallahassee, Florida 32310, United States

Dian-Teng Chen – Department of Physics, University of Florida, Gainesville, Florida 32611, United States

Khalil A. Abboud — Department of Chemistry, University of Florida, Gainesville, Florida 32611, United States

Hai-Ping Cheng – Department of Physics, University of Florida, Gainesville, Florida 32611, United States

Stephen Hill — National High Magnetic Field Laboratory and Department of Physics, Florida State University, Tallahassee, Florida 32310, United States; orcid.org/0000-0001-6742-3620

Complete contact information is available at: https://pubs.acs.org/10.1021/acs.inorgchem.0c00332

Notes

The authors declare no competing financial interest.

ACKNOWLEDGMENTS

This work was supported as part of the Center for Molecular Magnetic Quantum Materials, an Energy Frontier Research Center funded by the U.S. Department of Energy, Office of Science, Basic Energy Sciences under Award No. DE-SC0019330. Computations were performed at NERSC and UFRC. EPR measurements were performed at the National High Magnetic Field Laboratory, which is supported by the National Science Foundation (DMR-1644779) and the State of Florida.

REFERENCES

- (1) Tasiopoulos, A. J.; Wernsdorfer, W.; Moulton, B.; Zaworotko, M. J.; Christou, G. Template Synthesis and Single-Molecule Magnetism Properties of a Complex with Spin S=16 and a $[\mathrm{Mn_8O_8}]^{8+}$ Saddle-Like Core. *J. Am. Chem. Soc.* **2003**, *125*, 15274–15275.
- (2) Matatov-Meytal, Y. I.; Sheintuch, M. Catalytic Abatement of Water Pollutants. *Ind. Eng. Chem. Res.* **1998**, *37*, 309–326.
- (3) Stüber, F.; Font, J.; Fortuny, A.; Bengoa, C.; Eftaxias, A.; Fabregat, A. Carbon materials and catalytic wet air oxidation of organic pollutants in wastewater. *Top. Catal.* **2005**, *33*, 3–50.
- (4) Abecassis-Wolfovich, M.; Landau, M. V.; Brenner, A.; Herskowitz, M. Catalytic Wet Oxidation of Phenol with Mn-Ce-Based Oxide Catalysts: Impact of Reactive Adsorption on TOC Removal. *Ind. Eng. Chem. Res.* **2004**, *43*, 5089–5097.
- (5) Montini, T.; Melchionna, M.; Monai, M.; Fornasiero, P. Fundamentals and Catalytic Applications of CeO₂-Based Materials. *Chem. Rev.* **2016**, *116*, 5987–6041.
- (6) Tasiopoulos, A. J.; O'Brien, T. A.; Abboud, K. A.; Christou, G. Mixed Transition-Metal/Lanthanide Complexes at Higher Oxidation States: Heteronuclear Ce^{IV}–Mn^{IV} Clusters. *Angew. Chem., Int. Ed.* **2004**, *43*, 345–349.
- (7) Maayan, G.; Christou, G. 'Old' Clusters with New Function: Oxidation Catalysis by High Oxidation State Manganese and Cerium/ Manganese Clusters Using O₂ Gas. *Inorg. Chem.* **2011**, *50*, 7015.
- (8) (a) Mishra, A.; Tasiopoulos, A. J.; Wernsdorfer, W.; Abboud, K. A.; Christou, G. High-Nuclearity Ce/Mn and Th/Mn Cluster Chemistry: Preparation of Complexes with [Ce₄Mn₁₀O₁₀(OMe)₆]¹⁸⁺ and [Th₆Mn₁₀O₂₂(OH)₂]¹⁸⁺ Cores. *Inorg. Chem.* **2007**, *46*, 3105. (b) Tasiopoulos, A. J.; Milligan, P. L.; Abboud, K. A.; O'Brien, T. A.; Christou, G. Mixed Transition Metal—Lanthanide Complexes at High Oxidation States: Heteronuclear Ce^{IV}Mn^{IV} Clusters. *Inorg. Chem.* **2007**, *46*, 9678–9691. (c) Papatriantafyllopoulou, C.; Abboud, K. A.; Christou, G. Mn/Ce clusters from the use of pivalate and chelate ligands: Mn^{III}₈Ce^{IV}, Mn^{III}₂Ce^{IV}₂, and Mn^{III}₄Ce^{III}₂ products. *Polyhedron*

2013, *52*, 196. (d) Lampropoulos, C.; Thuijs, A. E.; Mitchell, K. J.; Abboud, K. A.; Christou, G. *Inorg. Chem.* **2014**, *53*, 6805–6816.

- (9) (a) Wang, H. S.; Ma, C. B.; Wang, M.; Chen, C. N.; Liu, Q. T. A Series of Complexes with a $[Mn_8O_8]^{8+}$ Saddle-like Core: Facile Synthesis, Crystal Structure and Magnetic Property. J. Mol. Struct. 2008, 875, 288-294. (b) Akhtar, M. N.; Lan, Y.; Aldamen, M. A.; Zheng, Y. Z.; Anson, C. E.; Powell, A. K. Effect of Ligand Substitution on the SMM Properties of Three Isostructural Families of Double-Cubane Mn₄Ln₂ Coordination Clusters. Dalton Trans. 2018, 47, 3485-3495. (c) Milios, C. J.; Wood, P. A.; Parsons, S.; Foguet-Albiol, D.; Lampropoulos, C.; Christou, G.; Perlepes, S. P.; Brechin, E. K. The Use of Methylsalicyloxime in Manganese Chemistry: A [Mn³_{III}] Triangle and Its Oxidation to a [Mn⁴_{IV} Ce²_{III}] Rod. Inorg. Chim. Acta 2007, 360, 3932-3940. (d) Romanenko, G. V.; Fursova, E. Y.; Ovcharenko, V. I. Structures of Cerium Manganese Pivalates. Russ. Chem. Bull. 2009, 58, 1-10. (e) Akhtar, M. N.; Lan, Y.; Mereacre, V.; Clérac, R.; Anson, C. E.; Powell, A. K. Synthesis, Structures and Magnetic Properties of Heterometallic Mn₂^{III} Ln₂^{III} Tetranuclear Complexes. Polyhedron 2009, 28, 1698-1703.
- (10) (a) Ma, C. B.; Hu, M. Q.; Chen, H.; Chen, C. N.; Liu, Q. T. A New Family of Homo- and Heterometallic Manganese Complexes at High Oxidation States Derived from the Oxidation of Mn^{II} with Ce^{IV}: Syntheses, Structures, and Magnetic Properties. Eur. J. Inorg. Chem. 2011, 2011, 5043-5053. (b) Wang, M.; Yuan, D. Q.; Ma, C. B.; Yuan, M. J.; Hu, M. Q.; Li, N.; Chen, H.; Chen, C. N.; Liu, Q. T. The Use of Phosphonates for Constructing 3d-4f Clusters at High Oxidation States: Synthesis and Characterization of Two Unusual Heterometallic CeMn Complexes. Dalton Trans. 2010, 39, 7276-7285. (c) Lan, T. X.; Zhang, X.; Chen, C. N.; Wang, H. S.; Wang, M.; Fan, Y. H. Synthesis and Electrocatalytic Reactivity for Water Oxidation of Two Cerium Complexes. J. Coord. Chem. 2018, 71, 1415-1429. (d) Najafpour, M. M.; Kozlevčar, B.; McKee, V.; Jagličić, Z.; Jagodič, M. The First Pentanuclear Heterobimetallic Coordination Cation with Ce^{III}, Ce^{IV} and Mn^{II}. Inorg. Chem. Commun. 2011, 14, 125-127. (e) Wang, G. C.; Sung, H. H. Y.; Dai, F. R.; Chiu, W. H.; Wong, W. Y.; Williams, I. D.; Leung, W. H. Heterometallic Cerium(IV) Perrhenate, Permanganate, and Molybdate Complexes Supported by the Imidodiphosphinate Ligand [N(i -Pr₂PO)₂]⁻. *Inorg.* Chem. 2013, 52, 2556-2563.
- (11) Malaestean, I. L.; Ellern, A.; Kögerler, P. $\{Ce_{10}Mn_8\}$: Cerium Analogues of the Decavanadate Archetype. *Eur. J. Inorg. Chem.* **2013**, 2013, 1635–1638.
- (12) Thuijs, A. E.; Marton, A.; Stamatatos, T. C.; Abboud, K. A.; Christou, G. High Nuclearity Cerium-Manganese Clusters and Their Structural and Magnetic Properties: Ce^{IV}₃Mn^{III}₇ and Ce^{IV}₅Mn^{III}₁₁. *Polyhedron* **2016**, *103*, 288–294.
- (13) Tasiopoulos, A. J.; Wernsdorfer, W.; Abboud, K. A.; Christou, G. A Reductive Aggregation Route to New $[Mn_{12}O_{12}(OMe)_2(O_2CPh)_{16}(H_2O)_2]^{2-}$ Single-Molecule Magnets Related to the $[Mn_{12}]$ Family. Angew. Chem., Int. Ed. 2004, 43, 6338–6342.
- (14) Lis, T. Preparation, structure, and magnetic properties of a dodecanuclear mixed-valence manganese carboxylate. *Acta Crystallogr. Sect. B: Struct. Crystallogr. Cryst. Chem.* **1980**, *B36*, 2042.
- (15) (a) King, P.; Wernsdorfer, W.; Abboud, K. A.; Christou, G. A Family of Mn₁₆ Single-Molecule Magnets from a Reductive Aggregation Route. *Inorg. Chem.* **2004**, *43*, 7315. (b) Tasiopoulos, A. J.; Wernsdorfer, W.; Abboud, K. A.; Christou, G. [Mn₁₂O₁₂(OMe)₂(O₂CPh)₁₆(H₂O)₂]²⁻ Single-Molecule Magnets and other Manganese Compounds from a Reductive Aggregation Procedure. *Inorg. Chem.* **2005**, *44*, 6324. (c) King, P.; Wernsdorfer, W.; Abboud, K. A.; Christou, G. Single-Molecule Magnets: A Reductive Aggregation Route to New Types of Mn₁₂ Complexes. *Inorg. Chem.* **2005**, *44*, 8659. (d) Tasiopoulos, A. J.; Wernsdorfer, W.; Abboud, K. A.; Christou, G. Two isomeric [Mn₁₂O₁₂(OMe)₂(O₂CPh)₁₆(H₂O)₂]²⁻ single-molecule magnets and a Mn^{III} polymer prepared by a reductive aggregation synthetic route. *Polyhedron* **2005**, *24*, 2505.

- (16) Thuijs, A. E.; King, P.; Abboud, K. A.; Christou, G. New Structural Types of Mn₁₆ Single-Molecule Magnets: W-Shaped Topology from Reductive Aggregation. *Inorg. Chem.* **2015**, *54*, 9127.
- (17) Vincent, J. B.; Folting, K.; Huffman, J. C.; Christou, G. Use of (NBu^a₄)[MnO₄] for inorganic syntheses in non-aqueous solvents. The preparation of a manganese(III) dimer containing bridging phenoxo oxygen atoms. *Inorg. Chem.* **1986**, 25, 996.
- (18) SHELXTL 2014; Bruker-AXS: Madison, WI, 2014.
- (19) Hassan, A. K.; Pardi, L. A.; Krzystek, J.; Sienkiewicz, A.; Goy, P.; Rohrer, M.; Brunel, L. C. Ultrawide band multifrequency high-field EMR technique: A methodology for increasing spectroscopic information. *J. Magn. Reson.* **2000**, *142*, 300–312.
- (20) Stoll, S.; Schweiger, A. EasySpin, a comprehensive software package for spectral simulation and analysis in EPR. *J. Magn. Reson.* **2006**, *178*, 42–55.
- (21) Kohn, W.; Sham, L. J. Self-Consistent Equations Including Exchange and Correlation Effects. *Phys. Rev.* **1965**, *140*, A1133.
- (22) Perdew, J. P.; Burke, K.; Ernzerhof, M. Generalized Gradient Approximation Made Simple. *Phys. Rev. Lett.* **1996**, 77, 3865–3868.
- (23) Bloechl, P. E. Projector Augmented-Wave Method. *Phys. Rev. B: Condens. Matter Mater. Phys.* 1994, 50, 17953.
- (24) Kresse, G.; Furthmuller, J. Efficiency of Ab-Initio Total Energy Calculations for Metals and Semiconductors Using a Plane-Wave Basis Set. *Comput. Mater. Sci.* **1996**, *6*, 15–50.
- (25) Kresse, G.; Furthmuller, J. Efficient Iterative Schemes for Ab Initio Total-Energy Calculations Using a Plane-Wave Basis Set. *Phys. Rev. B: Condens. Matter Mater. Phys.* **1996**, *54*, 11169–11186.
- (26) Loschen, C.; Carrasco, J.; Neyman, K. M.; Illas, F. First-Principles Lda Plus U and Gga Plus U Study of Cerium Oxides: Dependence on the Effective U Parameter. *Phys. Rev. B: Condens. Matter Mater. Phys.* **2007**, *75*, 035115.
- (27) Marzari, N.; Mostofi, A. A.; Yates, J. R.; Souza, I.; Vanderbilt, D. Maximally Localized Wannier Functions: Theory and Applications. *Rev. Mod. Phys.* **2012**, *84*, 1419.
- (28) Marzari, N.; Vanderbilt, D. Maximally Localized Generalized Wannier Functions for Composite Energy Bands. *Phys. Rev. B: Condens. Matter Mater. Phys.* **1997**, *56*, 12847–12865.
- (29) Bain, G. A.; Berry, J. F. Diamagnetic corrections and Pascal's constants. J. Chem. Educ. 2008, 85, 532.
- (30) Davidson, E. R. MAGNET; Indiana University: Bloomington, IN, 1999.
- (31) Davidson, E. R. GRID; Indiana University: Bloomington, IN, 1999.
- (32) (a) Brown, I. D.; Altermatt, D. Bond-Valence Parameters Obtained from a Systematic Analysis of the Inorganic Crystal Structure Database. *Acta Crystallogr., Sect. B: Struct. Sci.* 1985, 41, 244–247. (b) Brese, N. E.; O'Keeffe, M. Bond-Valence Parameters for Solids. *Acta Crystallogr., Sect. B: Struct. Sci.* 1991, 47, 192–197.
- (33) Mereacre, V.; Ako, A. M.; Akhtar, M. N.; Lindemann, A.; Anson, C. E.; Powell, A. K. Homo- and Hetereovalent Polynuclear Cerium and Cerium/Manganese Aggregates. *Helv. Chim. Acta* **2009**, 92, 2507–2524.
- (34) Hui-Sheng, W.; Zhi-Quan, P. Synthesis, Crystal Structure, and Magnetic Properties of Mn-Ce Mixed-Metal Complex Containing Benzoic Ligands. *Chin. J. Inorg. Chem.* **2013**, *29*, 1459–1464.
- (35) Chilton, N. F.; Anderson, R. P.; Turner, L. D.; Soncini, A.; Murray, K. S. J. PHI: A powerful new program for the analysis of anisotropic monomeric and exchange-coupled polynuclear d- and f-block complexes. *J. Comput. Chem.* **2013**, *34*, 1164–1175.
- (36) Mukherjee, S.; Stull, J. A.; Yano, J.; Stamatatos, T. C.; Pringouri, K.; Stich, T. A.; Abboud, K. A.; Britt, R. D.; Yachandra, V. K.; Christou, G. Synthetic model of the asymmetric [Mn₃CaO₄] cubane core of the oxygen-evolving complex of photosystem II. *Proc. Natl. Acad. Sci. U. S. A.* **2012**, *109*, 2257–2262.
- (37) Vleck, J. H. The Theory of Electric and Magnetic Susceptibilities; Oxford Press: London, 1932.
- (38) Kambe, K. On the paramagnetic susceptibilities of some polynuclear complex salts. *J. Phys. Soc. Jpn.* **1950**, *5*, 48–51.

- (39) Hill, S. Magnetization Tunneling in High-Symmetry Mn₁₂ Single-Molecule Magnets. *Polyhedron* **2013**, *64*, 128–135.
- (40) Marbey, J.; Gan, P. R.; Yang, E. C.; Hill, S. Magic-angle Effects in a Trigonal Mn^{III}₃ Cluster: Deconstruction of a Single-Molecule Magnet. *Phys. Rev. B: Condens. Matter Mater. Phys.* **2018**, 98, 144433.
- (41) Krzystek, J.; Ozarowski, A.; Telser, J. Multi-Frequency, High-Field EPR as a Powerful Tool to Accurately Determine Zero-Field Splitting in High-Spin Transition Metal Coordination Complexes. *Coord. Chem. Rev.* **2006**, 250, 2308–2324.
- (42) Hureau, C.; Blondin, G.; Cesario, M.; Un, S. Direct Measurement of the Hyperfine and g-Tensors of a Mn(III)–Mn(IV) Complex in Polycrystalline and Frozen Solution Samples by High-Field EPR. J. Am. Chem. Soc. 2003, 125, 11637–11645.
- (43) Wilson, A.; Lawrence, J.; Yang, E. C.; Nakano, M.; Hendrickson, D. N.; Hill, S. Magnetization Tunneling in High-Symmetry Single-Molecule Magnets: Limitations of the Giant Spin Approximation. *Phys. Rev. B: Condens. Matter Mater. Phys.* **2006**, 74, R140403.
- (44) Hill, S.; Datta, S.; Liu, J.; Inglis, R.; Milios, C. J.; Feng, P. L.; Henderson, J. J.; del Barco, E.; Brechin, E. K.; Hendrickson, D. N. Magnetic Quantum Tunneling: Insights from Simple Molecule-Based Magnets. *Dalton Trans.* **2010**, *39*, 4693–4707.
- (45) (a) Hill, S.; Edwards, R. S.; Aliaga-Alcalde, N.; Christou, G. Quantum Coherence in an Exchange-Coupled Dimer of Single-Molecule Magnets. *Science* **2003**, *302*, 1015–1018. (b) Liu, J.; Krzystek, J.; Barrios, L.; Hill, S.; Aromì, G. Elucidating Magnetic Exchange and Anisotropy in Weakly Coupled Mn^{III} Dimers. *Inorg. Chem.* **2013**, *52*, 718–723. (c) Nguyen, T.; Shiddiq, M.; Ghosh, T.; Abboud, K. A.; Hill, S.; Christou, G. Covalently Linked Dimer of Mn₃ Single-Molecule Magnets and Retention of Its Structure and Quantum Properties in Solution. *J. Am. Chem. Soc.* **2015**, *137*, 7160–7168.
- (46) Datta, S.; Bolin, E.; Inglis, R.; Milios, C. J.; Brechin, E. K.; Hill, S. A Comparative EPR Study of High- and Low-Spin Mn₆ Single-Molecule Magnets. *Polyhedron* **2009**, *28*, 1788–1791.
- (47) Thuijs, A. E.; Li, X.-G.; Wang, Y.-P.; Abboud, K. A.; Zhang, X.-G.; Cheng, H.-P.; Christou, G. Molecular Analogue of the Perovskite Repeating Unit and Evidence for a Direct Mn^{III}-Ce^{IV}-Mn^{III} Exchange Coupling Pathway. *Nat. Commun.* **2017**, *8*, 500.